Contrast-transfer improvement for electrode displacement elastography

Shyam Bharat[1,2] **and Tomy Varghese**[1,2]

[1] Department of Medical Physics, University of Wisconsin-Madison, 1300 University Avenue, 1530 MSC, Madison, WI 53706, USA
[2] Department of Electrical and Computer Engineering, University of Wisconsin-Madison, 1300 University Avenue, 1530 MSC, Madison, WI 53706, USA

E-mail: tvarghese@wisc.edu

Abstract

Electrode displacement elastography is a strain imaging method that can be used for *in-vivo* imaging of radiofrequency ablation-induced lesions in abdominal organs such as the liver and kidney. In this technique, tissue motion or deformation is introduced by displacing the same electrode used to create the lesion. Minute displacements (on the order of a fraction of a millimetre) are applied to the thermal lesion through the electrode, resulting in localized tissue deformation. Ultrasound echo signals acquired before and after the electrode-induced displacements are then utilized to generate strain images. However, these local strains depend on the modulus distribution of the tissue region being imaged. Therefore, a quantitative evaluation of the conversion efficiency from modulus contrast to strain contrast in electrode-displacement elastograms is warranted. The contrast-transfer efficiency is defined as the ratio (in dB) of the observed elastographic strain contrast and the underlying true modulus contrast. It represents a measure of the efficiency with which elastograms depict the underlying modulus distribution in tissue. In this paper, we develop a contrast-transfer efficiency formalism for electrode displacement elastography (referred to as contrast-transfer improvement). Changes in the contrast-transfer improvement as a function of the underlying true modulus contrast and the depth of the inclusion in the simulated phantom are studied. We present finite element analyses obtained using a two-dimensional mechanical deformation and tissue motion model. The results obtained using finite element analyses are corroborated using experimental analysis and an ultrasound simulation program so as to incorporate noise artifacts.

Introduction

Elastography is an imaging modality that involves the imaging of local strains incurred in tissue as a result of mechanical stimuli (Ophir *et al* 1991, Insana *et al* 2001, Varghese *et al* 2001, Hall *et al* 2003). Elastic properties of tissue are known to be correlated with pathological changes that occur in tissue (Fung 1981). Cancers like scirrhous carcinoma of the breast manifest as extremely hard nodules (Anderson 1953, Ponnekanti *et al* 1995, Krouskop *et al* 1998). Hence, manual palpation has been extensively used for detection of tumours in the breast and prostate. However, this method is rendered ineffective when the tumours are small in size and located deep in the body. Sonography has also been utilized for imaging the extent of abdominal lesions created using techniques such as radiofrequency (RF), microwave or high-intensity focused ultrasound (HIFU) ablations (Solbiati *et al* 1997a, 1997b, 2001). However, in many cases, lesions do not possess echogenic properties that differ from that of normal tissue, making them ultrasonically undetectable. For example, in spite of being significantly stiffer than surrounding normal tissue, tumours of the prostate may not be visible (isoechoic) in standard ultrasound examinations (Scheipers *et al* 2003). Also, similar acoustic backscatter properties of the lesion and normal tissue lead to poor contrast on B-mode images (Goldberg *et al* 1998, Goldberg 2001). Elastography is hypothesized to possess the ability to differentiate tumours or lesions from normal tissue with better contrast than currently achievable in existing imaging techniques.

External compression elastography, where tissue motion is induced using an external compression plate or by the ultrasound transducer itself, is the most common elastographic imaging technique (Ophir *et al* 1991, Insana *et al* 2001, Varghese *et al* 2001, Hall *et al* 2003). This method works well for superficial organs like the breast and prostate. However, in case of abdominal organs like the liver and kidneys that are not directly accessible, compression has to be applied through the skin, leading to non-uniform contact between the compressor and the body, which culminates in elastograms with low signal-to-noise ratio (SNRe) and contrast-to-noise ratio (CNRe). Other problems associated with imaging these organs using the external compression technique are excessive lateral and elevational motion caused both due to the compression process and physiological motion resulting from cardiovascular and respiratory processes (Kolen *et al* 2002, Varghese *et al* 2002a, 2002b). An alternative method of introducing motion or deformation in tissue is possible for monitoring the size and extent of lesions created using RF ablation (Varghese *et al* 2002b, Jiang *et al* 2007, Bharat *et al* 2005).

Elastography has been used in the imaging of coagulated regions created using ablative therapies (Stafford *et al* 1998, Righetti *et al* 1999, Wu *et al* 2001, Varghese *et al* 2002a, 2002b). RF ablation is a procedure where an electrode is placed into the area of tissue to be ablated for localized thermal therapy. Ionic agitation in the tissue adjacent to the electrically active region of the electrode causes intense localized heating, leading to instant tissue necrosis if the ablation temperature is greater than 60 °C (Solbiati *et al* 1997a). The resulting lesions are known to be significantly stiffer than the untreated regions, due to a process known as protein denaturation (Righetti *et al* 1999, Wu *et al* 2001, Varghese *et al* 2002b, 2003). This leads to the possibility of elastographic imaging of these lesions. Electrode displacement elastography can be used as an alternative to external compression elastography in this case, because of the imaging geometry. In this method, localized tissue motion is induced by applying minute displacements (on the order of a fraction of a millimetre) to the unconstrained end of the same electrode used to create the thermal lesion (Varghese *et al* 2002b, Jiang *et al* 2007, Bharat *et al* 2005). This method of tissue displacement offers the flexibility of performing elastographic imaging either during or immediately after the RF ablation procedure.

The resulting tissue motion or deformation due to electrode displacement is therefore localized and restricted to regions surrounding the RF electrode. In a recent study involving experiments on a single-inclusion tissue-mimicking (TM) phantom, we found that the observed strain contrast on the electrode-displacement elastograms was consistently higher than the known modulus contrast between the inclusion and the background (Bharat *et al* 2005). This was a departure from the previously described contrast-transfer efficiency (CTE) criterion (Ponnekanti *et al* 1995, Kallel *et al* 1996) for external compression elastography, where the observed elastographic strain contrast was always less than or equal to the underlying modulus contrast. The CTE for external compression elastography is defined as the ratio of the observed elastographic strain contrast and the true underlying modulus contrast, expressed in decibels (dB). Since the quantity mapped in elastograms is the internal stain incurred in tissue due to an external stimulus, the information depicted (strain) is not an inherent property of tissue, but is a function of the tissue characteristics (modulus) and the applied external stimulus (stress). The CTE provides a quantitative measure of this conversion from the underlying tissue modulus to the observed elastographic strains. Ponnekanti *et al* found that stiffer lesions in a softer background were displayed on elastograms with a higher CTE, as compared to softer lesions in a stiffer background (Ponnekanti *et al* 1995). Under all different contrast conditions, the CTE obtained was always less than 0 dB. An exception was the case where the true modulus contrast ratio between the lesion and the background was 1:1, where the CTE equalled 0 dB. In general, for stiffer lesions in a softer background, the observed strain contrast was close to the true modulus contrast, while for softer lesions in a stiffer background, the observed strain contrast was significantly lower than the actual modulus contrast. In this paper, we present a CTE formalism for electrode-displacement elastography (referred to as contrast-transfer improvement (CTI), to differentiate it from the term 'CTE' for external compression elastography) and compare results with that obtained for external compression elastography. We have included results from the finite element analysis (FEA) of two-dimensional tissue deformation for a simulated single inclusion phantom. The finite element analysis displacements are then incorporated into an ultrasound simulation program. Our simulation results are also corroborated by results obtained from phantom experiments.

Materials and methods

Finite element analysis

A commercial finite element analysis package, ANSYS (ANSYS Inc., Pittsburgh, PA, USA) was used for modelling the two-dimensional tissue deformation in response to the mechanical stimuli. The dimensions of the two-dimensional (2D) tissue phantom were 120 mm (height) × 40 mm (width). A single cylindrical inclusion with a radius of 8 mm was incorporated into the simulated phantom. This cylindrical inclusion was centred at different depths (20 mm, 40 mm, 60 mm, 80 mm and 100 mm from the surface of the ultrasound transducer) in the background of the tissue phantom. Each depth was studied as a separate case. An RF electrode, with a diameter of 1 mm, was embedded in the inclusion, with the lower end of the electrode extending 12 mm into the inclusion from the top surface of the phantom. Figure 1(a) shows a schematic representation of this model, with the inclusion centred at 40 mm from the upper surface of the tissue background in the simulated phantom, which also denotes the surface of the ultrasound transducer. A second 2D tissue phantom with dimensions 40 mm × 40 mm was also created for use in conjunction with a frequency-domain based ultrasound simulation program (Li and Zagzebski 1999). Details regarding this are provided in the next sub-section, where we will refer to this phantom as the 'modified' phantom.
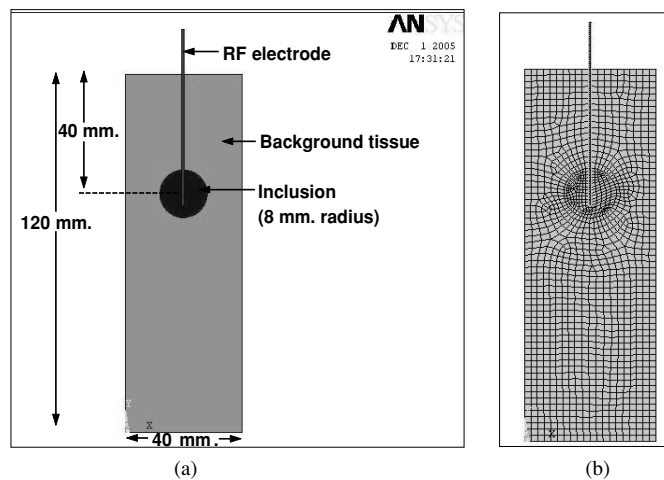
Figure 1. (a) The 2D ANSYS simulated phantom used to simulate RF electrode displacement. The displacements are applied to the upper unconstrained end of the RF electrode. (b) The nodal mesh created in ANSYS. The nodal displacements are used to calculate strains in the simulated phantom.

Table 1. The table presents the different moduli values used in the simulations and the resulting modulus contrast between the inclusion and the background.

Modulus of the inclusion (simulated lesion) in kPa	Modulus of the background in kPa	Underlying true modulus contrast 'C_t' (ratio of inclusion and background moduli)	Underlying true modulus contrast in dB ($20*\log_{10}C_t$)
1	10	1:10	−20
2	10	1:5	−13.9794
5	10	1:2	−6.0206
10	10	1:1	0
20	10	2:1	6.0206
50	10	5:1	13.9794
100	10	10:1	20

The mechanical properties of the simulated phantom were chosen such that the inclusion-background elastic moduli ratios and Poisson's ratios match previously published values for liver tissue (Emelianov *et al* 1998, Wen Chun *et al* 2002, Kiss *et al* 2004). Both soft inclusions in a stiffer background and stiffer inclusions in a soft background were simulated. Different known possibilities regarding the variations in tumour or inclusion stiffness were simulated. For example, hepatocellular carcinomas are known to be softer than a healthy liver (Wen Chun *et al* 2002), while haemangiomas appear as stiffer regions (when compared to healthy tissue) on strain images. This appearance on strain images is probably due to the stiffer outer shell that surrounds the softer haemangioma (Emelianov *et al* 1998). The elastic modulus of the background tissue (which models untreated tissue) was fixed at 10 kPa, while the elastic modulus of the inclusion was varied from 1 kPa to 100 kPa in finite steps, thus leading to inclusion–background moduli ratios ranging from 1:10 to 10:1, respectively. Table 1 lists the various moduli values used for the inclusion and the resulting inclusion–background moduli

ratios. Poisson's ratio for both treated tissue (inclusion) and untreated tissue (background) was fixed at 0.495, to model the incompressible nature of soft tissue (Jiang *et al* 2007). For the RF ablation electrode, Young's modulus and Poisson's ratio were chosen to be those for gold (78 GPa and 0.44 respectively), assuming gold as the electrode material (Panescu 1997).

The density of the mesh utilized for the ANSYS simulated phantom was varied in the phantom, with regions closer to the tip of the RF electrode meshed with comparatively higher density (to obtain fine displacement estimates), since the displacement applied to the unconstrained end of the electrode would result in greater displacements in regions closer to the electrode. On the other hand, the mesh applied to the background was coarser than that applied to the inclusion to improve the computational speed. In addition, the narrow width of the electrode made it imperative that the electrode be meshed with a fine mesh as well. The meshed tissue model is illustrated in figure 1(b).

The ultrasound transducer used for imaging was assumed to be in the same plane as the RF electrode, in contact with the upper surface of the tissue model. Hence, for the 2D case, only the nodes belonging to the background and inclusion (and not the electrode) were selected for further processing to obtain axial strain images. Tissue motion was induced by applying minute displacements (not greater than 2.4 mm) to the unconstrained end (top end) of the RF electrode. The displacement can be either towards or away from the transducer. Implicit in this technique is the assumption that part of the tissue in contact with the electrode is always bound to the electrode. This has been shown to be the case with RF ablation and described in the literature (Mikami *et al* 2004), where it was found that, during RF ablation, protein destruction and carbonization occurring around the electrically active region of the ablation electrode causes adhesion between the electrode and the ablated tissue (i.e. the inclusion in our simulated phantom). In addition, there is no adhesion between the electrode and the background (which corresponds to untreated tissue after the ablation procedure). The contact interaction between the background and the electrode is entirely governed by the coefficient of friction between the electrode and the background (Serway 1990). We found in our simulations that varying the coefficient of friction from 0.01 to 0.99 does not significantly affect the strain contrast and subsequently the CTI of the resulting strain images. The statistical significance in the dependence of the CTI on the coefficient of friction was evaluated using a paired *t*-test and the *p*-value obtained was 0.0984, indicating that the CTI in electrode displacement elastography does not depend on the coefficient of friction.

The different boundary conditions associated with the displacement of the RF electrode towards and away from the transducer are discussed below. For the case where the RF electrode displacement is moved towards the transducer, the ultrasound transducer constrains the motion of the upper boundary of the simulated tissue phantom in the vertical direction (Jiang *et al* 2007). In addition, since the applied displacement causes localized motion, we assume that the sides and bottom of the simulated phantom do not move. For the case of RF electrode displacement away from the transducer, all the above boundary conditions remain the same except that for the upper surface of the simulated phantom which is in contact with the transducer. Since the transducer in this case does not constrain the upper surface, the vertical constraint for this surface is relaxed (Jiang *et al* 2007).

The axial nodal displacements resulting from a 0.6 mm perturbation of the electrode were fed into a linear least squares program for strain calculation, implemented in Matlab (The MathWorks, Natick, MA, USA), after performing bilinear interpolation to obtain displacement estimates in a regular 2D Cartesian matrix format. For the ideal FEA strain images, the trends in CTI were evaluated for different underlying modulus contrasts between the inclusion and background (10:1, 5:1, 2:1, 1:1, 1:2, 1:5 and 1:10) and for different inclusion depths (20 mm, 40 mm, 60 mm, 80 mm and 100 mm from the surface of the ultrasound transducer).

All these cases were studied for RF electrode displacement both towards and away from the ultrasound transducer. The external compression CTE values for different underlying true modulus contrasts were obtained from the results published by Ponnekanti *et al* (1995).

Ultrasound simulation program

In addition to evaluating the ideal strain images obtained from the axial displacements resulting from the FEA, we evaluated the contribution of ultrasonic speckle to the CTI. An ultrasound simulation program was used to simulate pre- and post-displacement RF data based on the FEA displacement data. In our simulations, we used a frequency-domain ultrasound simulation program developed by Li and Zagzebski (1999). The inputs to this program were the lateral and axial displacement fields from ANSYS, after appropriate interpolation to a regular Cartesian grid. A 128 element linear array transducer consisting of 0.15 mm × 10 mm elements with a 0.2 mm centre-to-centre separation was used in the simulation. Gaussian shaped incident pulses with a centre frequency of 10 MHz and an 80 % bandwidth (full-width at half-maximum) were modelled. Scatterers in the medium were modelled using 100 μm radius polystyrene beads, which were randomly distributed in the phantom at a high enough number density (per resolution cell) to ensure Rayleigh scattering (Wagner *et al* 1983). Finally, the speed of sound for the phantom was assumed to be 1540 m s^{-1} and attenuation effects were ignored to minimize computational complexity. The pre- and post-displacement RF data from this simulation program were compared using a one-dimensional (1D) cross-correlation program in Matlab to calculate the axial displacement field. A linear least squares method was used to calculate the axial strain distribution. This axial strain map obtained constitutes the 'simulated' strain images, which are compared with the ideal FEA strain images obtained earlier.

To reduce the computational time, the 'modified' phantom mentioned earlier was used and the nodal displacements from this modified ANSYS-simulated phantom were used in the ultrasound simulation program. Eight independent runs of the ultrasound simulation were carried out to generate errorbars for comparison with the FEA-generated results. Figure 2(a) shows a simulated B-mode image for an 8 mm radius cylindrical inclusion centred at 20 mm in a 40 mm × 40 mm phantom. Figures 2(b) and (c) show corresponding strain images from the FEA and ultrasound simulation, respectively. The changes in CTI at different true inclusion–background modulus contrasts were used for comparison between the ideal and simulated strain images.

Tissue-mimicking phantom

The CTI values obtained from FEA-generated strain images were also validated using CTI values obtained from experimental strain images of a custom-made tissue mimicking (TM) phantom. A schematic diagram of the TM phantom for electrode displacement elastography is shown in figure 3. The TM materials used in the phantom have been described previously (Madsen *et al* 2003) and consist of dispersions of microscopic safflower oil droplets in a gelatin matrix. The 19 mm diameter spherical inclusion was formed and bonded around the hooked end of a stainless steel rod, the latter representing an ablation electrode. A storage modulus (real part of the complex Young's modulus) of 50 ± 2 kPa was measured at 1 Hz for the inclusion material using a Bose EnduraTEC® model 3200 system (Madsen *et al* 2005). Surrounding the inclusion and bonded to it is the background material with a storage modulus of 11 ± 2 kPa. Thus, the inclusion is approximately five times stiffer than the background. Oil droplets in both materials provide tissue-like ultrasonic backscatter and attenuation. The inclusion is centred in the 12 cm × 12 cm × 12 cm cube of background material.
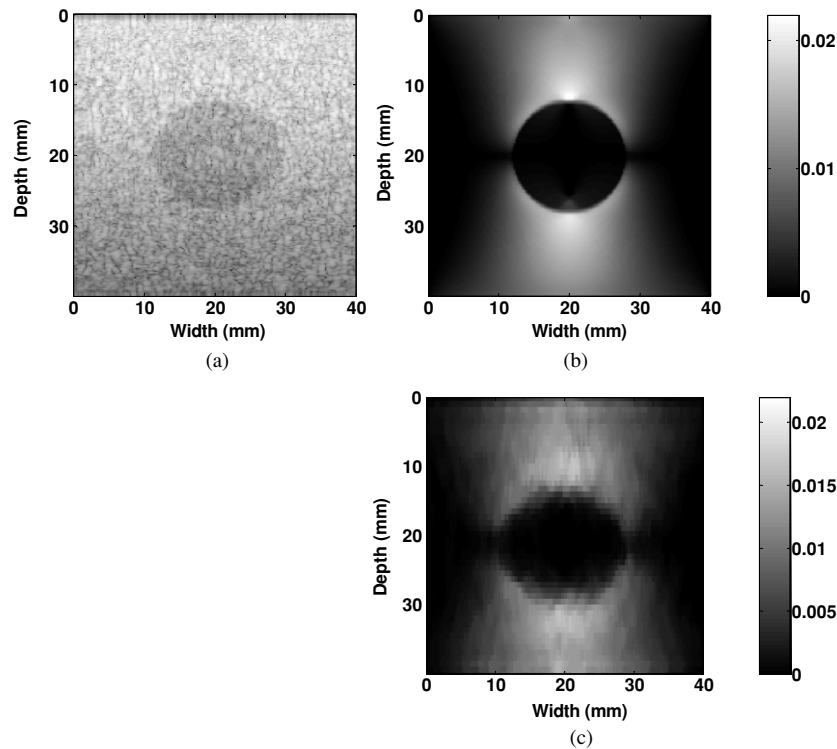
Figure 2. (a) B-mode image from the US simulation program. (b) Ideal strain image obtained from FEA-generated displacements. (c) Simulated strain image, obtained using pre- and post-displacement data gathered from the US simulation program.

To generate elastograms, the simulated electrode was displaced vertically using a stepper motor system, producing a maximum displacement of 0.2 mm. Two real-time ultrasound scanners, namely an Ultrasonix 500RP (Ultrasonix Medical Corporation, Bothell, WA, USA) and an Aloka SSD 2000 (Aloka, Tokyo, Japan), were used to acquire RF data. Linear array transducers having a centre frequency of 5 MHz were used. The Ultrasonix transducer has a 49 mm footprint with a 60% bandwidth, while the transducer used with the Aloka SSD 2000 system has a 40 mm footprint with a 70% bandwidth. In the case of the Ultrasonix 500RP system, digitization of RF echo signals was performed internally at a 40 MHz sampling frequency, while for the Aloka SSD 2000 system, digitization was performed using an external 12-bit data acquisition board (Gage, Montreal, QC, Canada) at a sampling rate of 100 MHz.

The ultrasound transducer was placed adjacent to the electrode, in a plane approximately parallel to that of the electrode as shown in figure 3. Pre- and post-displacement RF data were acquired for two different displacement conditions: (1) displacement of the RF electrode (inclusion) away from the ultrasound transducer and (2) displacement of the RF electrode (inclusion) towards the ultrasound transducer, the latter following an initial displacement of 0.25 mm away from the transducer. Ten independent data sets were acquired for a 0.2 mm displacement, for both the above-mentioned data acquisition methods. Higher displacements of the electrode were avoided so as to prevent damage by way of loss of bonding of the inclusion to the hooked end of the electrode. The ten data sets were acquired by rotating the ultrasound transducer around the electrode and recording one data set for a particular
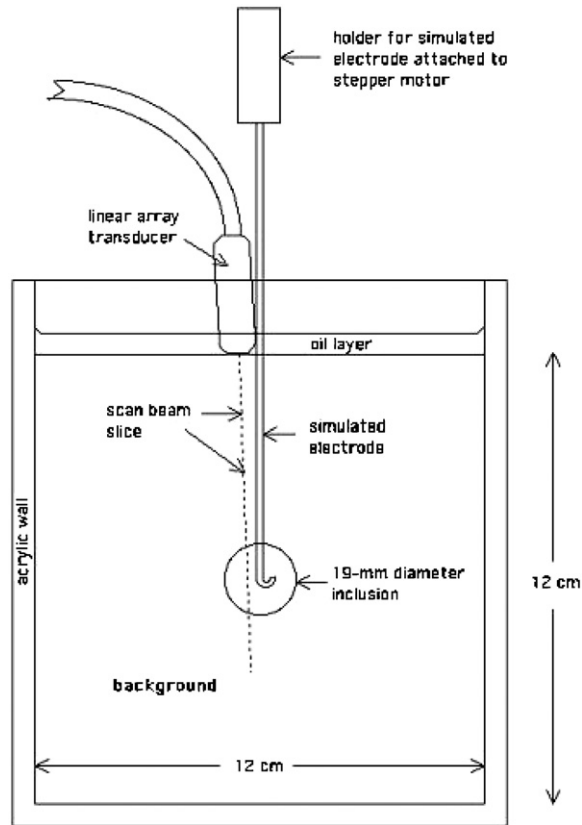
Figure 3. Experimental set-up showing the single-spherical inclusion phantom with an electrode embedded in the inclusion. RF electrode displacement for elastography is induced by applying precise, stepper-motor controlled displacements to the upper unconstrained end of the electrode. Pre- and post-displacement raw RF data are collected using the ultrasound transducer positioned adjacent to the electrode.

orientation of the transducer with respect to the electrode to obtain independent data sets. Again, a 1D cross correlation algorithm in conjunction with a linear least-squares method was used to estimate axial strains resulting from the electrode perturbations.

Computation of the CTI

Ponnekanti *et al* described the CTE as the ratio of the observed elastographic strain contrast and the true underlying modulus contrast, for external compression elastography (Ponnekanti *et al* 1995). Mathematically, it is given by the following equations:

$$\text{CTE} = \frac{C_o}{C_t} \tag{1}$$

$$\text{In dB, CTE}(dB) = C_o(dB) - C_t(dB) \tag{2}$$

where C_o is the observed elastographic strain contrast and C_t is the true underlying modulus contrast. In this case, contrast is defined to be between the inclusion and the background.
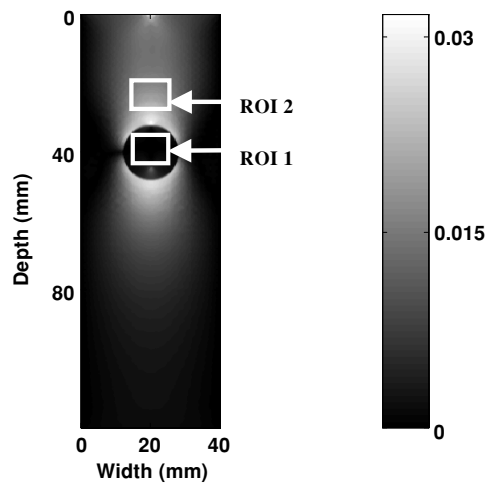
Figure 4. Illustration of the CTI computation using pixel values from the regions of interest (ROIs) shown on the strain image.

Mathematically, the expression for the CTI is the same as that for the CTE (equations (1) and (2)). For calculating the values of C_o under different conditions, rectangular regions of interest (ROIs) were selected within the inclusion and in the background, as shown in figure 4. The main difference in the method of CTI calculation for electrode displacement elastography versus CTE for external compression elastography is the selection of the ROI in the background. Ponnekanti *et al* used the mean value of all the background strain pixels in the absence of the inclusion as an estimate of the background strain (Ponnekanti *et al* 1995), whereas we use a rectangular ROI (ROI 2) to calculate the value of background strain to be used in the strain contrast calculation. The reasoning behind the choice of ROI 2 is presented in the next paragraph. The ratio of the mean pixel value in ROI 2 and the mean pixel value in ROI 1 is then taken to be the value of C_o. ROI 1 within the inclusion was chosen so as to maximize the number of pixels used for calculation, subject to the constraint that they lay within the inclusion.

An important characteristic of the electrode displacement method is the localized nature of the displacements. As observed in figure 4, the local strains or displacements to the right and left side of the inclusion are very small. We did not choose our background ROI (ROI 2) to lie in these regions of low strain, as they would not then accurately represent the background strain. This precluded the use of all background pixels in the calculation of the background strain and necessitated the use of an ROI. Regarding the choice of the ROI location, this left the regions above and below the inclusion as possible locations for ROI 2. The region for the ROI 2 in the background was selected slightly above the inclusion, as illustrated in figure 4. However, a similar region can also be selected below the inclusion. The other parameter to be selected was the position of the background ROI 2 above the inclusion. We chose ROI 2 to be as close to the inclusion as possible, while avoiding the regions of high strain values just above the inclusion. Since these regions have increased strain, they could suffer from increased decorrelation resulting from higher (or possibly lateral) displacements that could not be tracked by the algorithm for the simulated and experimental elastograms. The reason for choosing a location near the inclusion for ROI 2 is because the visual contrast demarcation is generally made by the human eye for regions located close to each other.
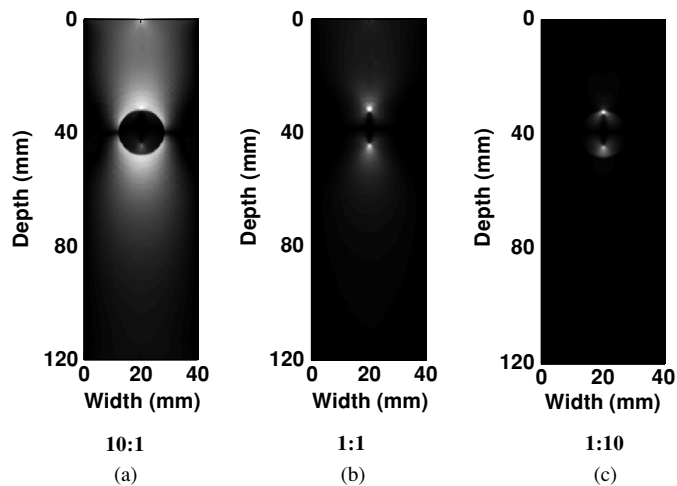
Figure 5. Ideal strain images obtained from FEA-generated displacements, for different inclusion–background modulus contrasts of (a) 10:1, (b) 1:1 and (c) 1:10, respectively.

The true modulus contrast, C_t, is obtained from the modulus values of the inclusion and the background that is input to the ANSYS simulated phantom.

The CTI describes the mechanical efficiency with which the strain elastograms depict the underlying modulus distribution. If the applied stress field is uniform throughout the phantom, then the relationship between the modulus and the strain would be linear, and we would expect a CTI of 1 (or 0 dB) when the moduli of the inclusion and the background are the same (similar to the CTE for external compression elastography).

Results

The trends in CTI were studied as a function of true modulus contrast and inclusion depth within the simulated phantom, for RF electrode displacement both towards and away from the ultrasound transducer. Figure 5 shows sample strain images generated using local displacements obtained from the FEA simulations, for the three different inclusion–background modulus contrasts, namely 10:1, 1:1 and 1:10. Figure 6 illustrates the trends in CTI as a function of different underlying modulus contrasts. The horizontal axis (*x*-axis) is the underlying modulus contrast of the inclusion and background. The vertical axis (*y*-axis) stands for CTI values corresponding to different modulus contrasts. All data points to the left of the $x = 0$ plane represent CTI values for softer inclusions in a stiffer background, while all data points to the right of the $x = 0$ plane represent CTI values for stiffer inclusions in a softer background. This plot displays CTI results from the 120 mm × 40 mm FEA simulated phantom, for the inclusion centred at 40 mm from the transducer and a 0.6 mm displacement of the electrode both towards and away from the transducer.

Figure 6 also shows the CTE values corresponding to the external compression method (Ponnekanti *et al* 1995, Kallel *et al* 1996). Note that the CTI trend for electrode displacement elastography follows the CTE curve for external compression elastography, for the case of softer inclusions in a stiffer background. In other words, the curves are similar to the left of the 0 dB point on the *x*-axis. However, in the case of stiffer inclusions in a softer background, the CTI values for electrode displacement elastography are significantly higher
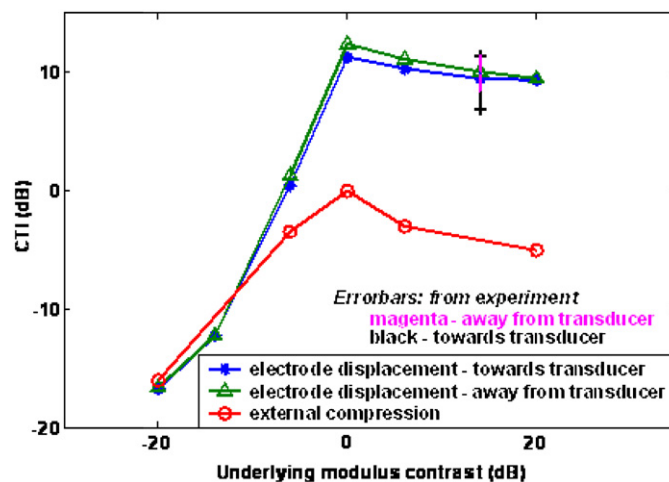
Figure 6. The variation in CTI for different true modulus contrasts is shown here. The strain images used to calculate the CTI are obtained from FEA-generated displacements. Two cases for electrode displacement (ED) elastography are shown, namely RF electrode displacement towards and away from the transducer. CTE data for external compression (EC) elastography are provided as a measure for comparison. Also, the standard error for the experimental CTI (for strain images obtained from the TM phantom) is shown superimposed on the graph for CTI from FEA-generated strain images. The two different errorbars shown correspond to the standard deviation for the cases of RF electrode displacement towards and away from the transducer.

(This figure is in colour only in the electronic version)

than the corresponding CTE for external compression elastography. CTI values for both the displacement directions in electrode displacement elastography are fairly similar, for all values of the underlying modulus contrast. Figure 6 also displays a comparison between the CTI values for the FEA and experimental strain images, which will be discussed later.

Figure 7 shows the CTI results obtained using the ultrasound simulation program as errorbars resulting from eight independent realizations for each value of the modulus contrast. The results here represent both RF electrode displacement towards the transducer (figure 7(a)) and RF electrode displacement away from the transducer (figure 7(b)). The solid lines in the plots represent CTI values from FEA-generated strain images. The FEA simulated phantom used had dimensions of 40 mm × 40 mm, where the displacements obtained after the RF electrode displacement was utilized in the ultrasound simulation program. The errorbars denotes the variation in the CTI, computed from the strain images using the ultrasound simulated data. The plots show good agreement between the CTI values for FEA and simulated strain images, for both directions of RF electrode displacement.

Figure 8 presents plots of the variation in CTI as a function of the depth of the inclusion. Note that the CTI value progressively decreases as a function of the inclusion depth. Observe that shallower inclusions have a higher CTI value than deeper inclusions. Figures 6 and 9 provide a comparison between the CTI values for the FEA and experimental strain images. Since the experimental phantom used had a modulus contrast of approximately 5:1 between the inclusion and the background, only one value of the modulus contrast was compared. Figure 6 shows a superimposition of the experimental CTI phantom results on the CTI plot for ideal strain images. The errorbars represent results from ten independent experiments, as discussed in the 'materials and methods' section. Results corresponding to both directions
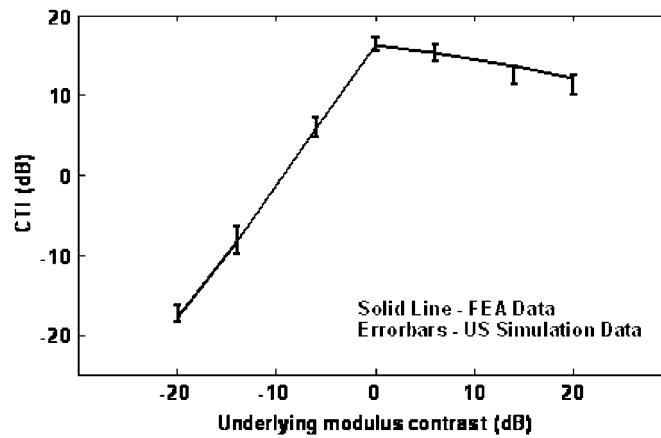
(a)
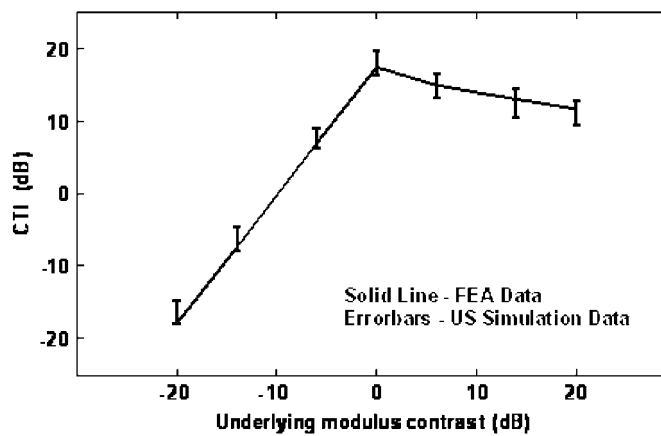
(b)

Figure 7. Comparison of CTI versus modulus contrast for ideal and simulated strain images. The solid line represents CTI values from ideal (FEA-generated) strain images and the errorbars represent fluctuations in the CTI parameter for eight independent simulated strain images obtained from ultrasound pre- and post-displacement echo signals. (a) RF electrode displacement towards transducer; (b) RF electrode displacement away from transducer.

of displacement are included in the figure. Figure 9 provides a bar plot of the CTI results corresponding to the two different ultrasound systems utilized and for both directions of the RF electrode displacement.

Discussion

The changes in the CTI for electrode displacement elastography as a function of underlying modulus contrast and depth of the inclusion in the simulated phantom were studied in this paper. It has been demonstrated that stiffer inclusions in a softer background are represented on strain images with much better efficiency (in other words, they have a higher CTI value) than softer inclusions in a stiffer background. This result is consistent with that of Ponnekanti *et al*
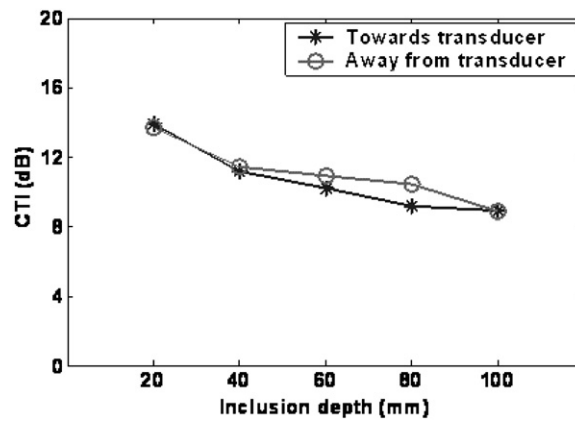
Figure 8. The changes in CTI as a function of the depth of the inclusion, where the location of the inclusion is progressively varied in finite steps from a depth of 20 mm (closest to the surface) to a depth of 100 mm (farthest from the surface). The strain images used to calculate the CTI are obtained from FEA-generated displacements.
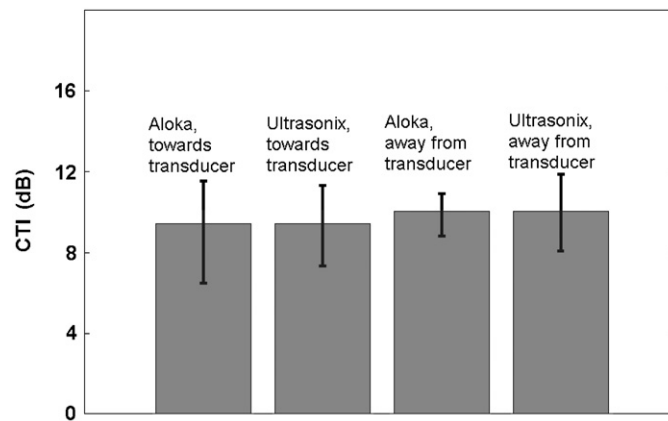

Figure 9. Bar graph showing the variations in CTI for data collected using two different ultrasound systems and for both directions of displacement. The height of the solid bars represents the CTI value for ideal strain images, while the errorbars represent standard deviation of experimental CTI values for each case.

(1995), who found similar characteristics for the CTE in external compression elastography. These results can be traced back to an important finding made in the mid-1950s, when it was found that softer inclusions in a stiffer background appear stiffer than they really are, albeit when Poisson's ratio is non-zero (Hueter and Bolt 1955). Since we assume Poisson's ratio of 0.495 to simulate the incompressibility property of tissue, the low CTI for softer inclusions in a stiffer background can be attributed to this effect (Ponnekanti *et al* 1995). Intuitively, these trends can be understood by observing figures 5(a)–(c). A stiffer inclusion in a softer background (10:1 modulus contrast, figure 5 (a)) can be visually delineated much better on the elastogram than a softer inclusion in a stiffer background (1:10 modulus contrast, figure 5(c)). Another apparent similarity between electrode displacement and external compression elastography is that the CTI curve peaks at a 0 dB modulus contrast. Also,

low contrast inclusions are represented on strain images with higher CTI than corresponding high contrast inclusions.

Though the above-mentioned similarities in the CTI and CTE trend exist for electrode displacement and external compression elastography, respectively, a significant difference in the absolute values of the CTI/CTE parameter for both methods can be clearly visualized. In external compression elastograms, the maximum CTE value reached is 0 dB (at 0 dB true modulus contrast), while electrode displacement elastograms have CTI values much in excess of 0 dB (approximately 10–15 dB for stiffer inclusions). In other words, this is representative of the fact that, in electrode displacement elastography, the elastographic strain contrast is actually higher than the true underlying modulus contrast. We first observed this effect in our laboratory, while performing experiments on the specially constructed TM phantom for electrode displacement elastography (Bharat *et al* 2005). A possible explanation for this effect may lie in the mode of tissue perturbation utilized for electrode displacement elastography. Since displacements are applied only to the RF electrode and not uniformly over the entire simulated phantom surface (as in external compression elastography), the resulting tissue motion is restricted to regions in contact with the electrode along its path in tissue. This results in higher strains in regions adjacent to the electrode and a reduction in strain as we move away from the electrode in a direction perpendicular to the electrode. Hence, viable strain or displacement information is only available in the regions close to the electrode. This entailed utilizing the higher strain regions, as shown in figure 4, to represent 'background strain' and effectively resulted in a higher elastographic strain contrast and subsequent CTI estimate. Having said so, these increased strains above and below the inclusion improve lesion detection in a clinical set-up, as it provides added contrast even for low-contrast situations. For example, a lesion which is only twice as stiff as the surrounding normal tissue may show up on an electrode displacement elastogram with a much higher strain contrast, leading to more efficient detection (in terms of the strain contrast or the CTI) and in boundary delineation.

As mentioned earlier, the electrode was displaced by 0.6 mm in our simulations. Higher displacements of the RF electrode would increase the localized displacement and deformation of the inclusion resulting in increased signal decorrelation, similar to that observed with external compression elastography. Larger displacements in our phantom experiments were restricted due to the possibility of damaging the phantom in terms of the loss of bonding contact between the electrode and the TM material. Similarly, in clinical situations, increased displacements would lead to loss of contact between the electrically active regions of the electrode and the ablated tissue, which would in turn render this method ineffective.

The depth of the inclusion has an impact on the CTI parameter, with shallower inclusions having higher CTI values than deeper inclusions. The effect of this decrease in the CTI with depth, however, is not visually discernable in the strain images. The decrease in CTI with depth is due to the reduced effective force (stress) on the inclusion. Since the external force is only applied at the upper end of the electrode, the effective force transmitted to the inclusion is lower for deeper inclusions. This was confirmed independently by FEA simulations where the length of the RF electrode was varied, while the depth of the inclusion was maintained constant. A paired *t*-test was utilized to characterize the depth-dependence of the CTI. The *p*-value obtained was 0.0159. Since the *p*-value is less than 0.05, we concluded that the drop in CTI as a function of inclusion depth is significant. Lastly, although our simulations did not incorporate ultrasonic attenuation effects, it must be noted that increased attenuation would lead to a lower sonographic signal-to-noise ratio (SNRs) resulting in reduced SNRe in strain images of inclusions at greater depths (18–20 cm) (Varghese and Ophir 1997).

The CTI results presented in this paper are also corroborated with the experimentally obtained values of the CTI, for the modulus contrast obtained with the TM phantom, which

compared favourably with the values obtained from FEA-strain images. Paired t-tests utilized to analyse the statistical significance of the dependence of the TM phantom CTI values on the direction of electrode displacement (towards versus away from the transducer) and on the ultrasound system used for data acquisition (Aloka SSD 2000 versus Ultrasonix 500RP) provide p-values of 0.3617 (direction of electrode displacement) and 0.8442 (ultrasound system used), respectively. Since the p-values obtained are greater than 0.05, we conclude that the CTI does not depend either on the direction of electrode displacement or on the ultrasound system used for data acquisition.

Conclusion

In this paper, we quantify the maximum strain contrast obtainable using electrode displacement elastography from the underlying modulus contrast distributions in tissue. This concept, referred to as the contrast-transfer improvement with electrode displacement elastography, was previously developed as contrast-transfer efficiency for external compression elastography. We illustrate in this paper that, for electrode displacement elastography, similar trends in the CTI parameter as seen in CTE for external compression elastography are observed at different underlying modulus contrasts. However, the electrode displacement method exhibits significantly higher absolute CTI values for stiffer inclusions embedded in a softer background (significantly greater than 0 dB) when compared to external compression elastography. This higher value of the CTI translates to increased contrast in the strain domain, higher than that originally present in the modulus domain, for electrode displacement elastography. This property of electrode displacement elastography could be useful for clearly delineating the boundaries of lesions or tumours that are slightly stiffer than surrounding normal tissue, since the observed strain contrast would be higher than the actual modulus contrast. In addition, we also demonstrate that the CTI obtained decreases as the depth of the inclusion from the surface of the transducer increases. The experimental TM phantom results presented in the paper also provide validation of the FEA-generated CTI values.

References

Anderson W A D 1953 *Pathology* (St Louis, MO: Mosby)

Bharat S, Madsen E L, Zagzebski J A and Varghese T 2005 Radiofrequency electrode displacement elastography—a phantom study *4th Int. Conf. on the Ultrasonic Measurement and Imaging of Tissue Elasticity* (Austin, TX, 2005)

Emelianov S Y, Rubin J M, Lubinski M A, Skovoroda A R and O'Donnell M 1998 Elasticity imaging of the liver: is a hemangioma hard or soft? *1998 IEEE Ultrasonics Symp. (Sendai, Japan)* ed S C Schneider, M Levy and B R McAvoy

Fung Y G 1981 *Biomechanical Properties of Living Tissues* (New York: Springer) chapter 7

Goldberg S N 2001 Radiofrequency tumor ablation: principles and techniques *Eur. J. Ultrasound* **13** 129–47

Goldberg S N, Gazelle G S, Solbiati L, Livraghi T, Tanabe K K, Hahn P F and Mueller P R 1998 Ablation of liver tumors using percutaneous RF therapy *AJR Am. J. Roentgenol.* **170** 1023–8

Hall T J, Zhu Y and Spalding C S 2003 *In vivo* real-time freehand palpation imaging *Ultrasound Med. Biol.* **29** 427–35

Hueter T F and Bolt R H 1955 *Sonics* (New York: Wiley)

Insana M F, Hall T J, Chaturvedi P and Kargel C 2001 Ultrasonic properties of random media under uniaxial loading *J. Acoust. Soc. Am.* **110** 3243–51

Jiang J, Varghese T, Chen Q, Hall T J and Zagzebski J A 2007 Finite element analysis of tissue deformation with a radiofrequency ablation electrode for strain imaging *IEEE Trans. Ultrason. Ferroelectr. Freq. Control* at press

Kallel F, Bertrand M and Ophir J 1996 Fundamental limitations on the contrast-transfer efficiency in elastography: an analytic study *Ultrasound Med. Biol.* **22** 463–70

Kiss M Z, Varghese T and Hall T J 2004 Viscoelastic characterization of in vitro canine tissue *Phys. Med. Biol.* **49** 4207–18

Kolen A F, Bamber J C and Ahmed E E 2002 Analysis of cardiovascular induced liver motion for application to elasticity imaging of the liver *in vivo J. Ultrasound Med.* **21** S53 (Abstract)

Krouskop T A, Wheeler T M, Kallel F and Hall T 1998 The elastic moduli of breast and prostate tissues under compression *Ultrason. Imaging* **20** 260–74

Li Y and Zagzebski J A 1999 Frequency domain model for generating B-mode images with array transducers *IEEE Trans. Ultrason. Ferroelectr. Freq. Control* **46** 690–9

Madsen E L, Frank G R, Krouskop T A, Varghese T, Kallel F and Ophir J 2003 Tissue-mimicking oil-in-gelatin emulsions for use in heterogeneous elastography phantoms *Ultrason. Imaging* **25** 17–38

Madsen E L, Hobson M A, Shi H, Varghese T and Frank G R 2005 Tissue-mimicking Agar/gelatin Materials for use in Heterogeneous Elastography Phantoms *Phys. Med. Biol.* **50** 5597–618

Mikami T and T A and H K 2004 Performance of bipolar forceps during coagulation and its dependence on the tip material: a quantitative experiment assay *Neurosurgery* **100** 133–8

Ophir J, Cespedes I, Ponnekanti H, Yazdi Y and Li X 1991 Elastography: a quantitative method for imaging the elasticity of biological tissues *Ultrason. Imaging* **13** 111–34

Panescu D 1997 Intraventricular electrogram mapping and radiofrequency cardiac ablation for ventricular tachycardia *Physiol. Meas.* **18** 1–38

Ponnekanti H, Ophir J, Yijun H and Cespedes I 1995 Fundamental mechanical limitations on the visualization of elasticity contrast in elastography *Ultrasound Med. Biol.* **21** 533–43

Righetti R, Kallel F, Stafford R J, Price R E, Krouskop T A, Hazle J D and Ophir J 1999 Elastographic characterization of HIFU-induced lesions in canine livers *Ultrasound Med. Biol.* **25** 1099–113

Scheipers U, Ermert H, Sommerfeld H J, Garcia-Schurmann M, Senge T and Philippou S 2003 Ultrasonic multifeature tissue characterization for prostate diagnostics *Ultrasound Med. Biol.* **29** 1137–49

Serway R A 1990 *Physics for Scientists and Engineers* 3rd edn (Philadelphia, PA: Saunders)

Solbiati L, Goldberg S N, Ierace T, Livraghi T, Meloni F, Dellanoce M, Sironi S and Gazelle G S 1997a Hepatic metastases: percutaneous radio-frequency ablation with cooled-tip electrodes *Radiology* **205** 367–73

Solbiati L *et al* 1997b Percutaneous US-guided radio-frequency tissue ablation of liver metastases: treatment and follow-up in 16 patients *Radiology* **202** 195–203

Solbiati L, Ierace T, Tonolini M, Osti V and Cova L 2001 Radiofrequency thermal ablation of hepatic metastases *Eur. J. Ultrasound* **13** 149–58

Stafford R J, Kallel F, Price R E, Cromeens D M, Krouskop T A, Hazle J D and Ophir J 1998 Elastographic imaging of thermal lesions in soft tissue: a preliminary study *in vitro Ultrasound Med. Biol.* **24** 1449–58

Varghese T and Ophir J 1997 The nonstationary strain filter in elastography: I. Frequency dependent attenuation *Ultrasound Med. Biol.* **23** 1343–56

Varghese T, Ophir J, Konofagou E, Kallel F and Righetti R 2001 Tradeoffs in elastographic imaging *Ultrason. Imaging* **23** 216–48

Varghese T, Techavipoo U, Liu W, Zagzebski J A, Chen Q, Frank G and Lee F T Jr 2003 Elastographic measurement of the areas and volumes of thermal lesions resulting from radiofrequency ablation: pathologic correlation *AJR Am. J. Roentgenol.* **181** 701–7

Varghese T, Zagzebski J A and Lee F T Jr 2002b Elastographic imaging of thermal lesions in the liver *in vivo* following radiofrequency ablation: preliminary results *Ultrasound Med. Biol.* **28** 1467–73

Varghese T, Zagzebski J A, Techavipoo U and Chen Q 2002a Elastographic Imaging of *in-vivo* soft tissue *US Patent* P02153US

Wagner R F, Smith S W, Sandrik J M and Lopez H 1983 Statistics of speckle in ultrasound B-scans *IEEE Trans. Sonics Ultrason.* **30** 156–63

Wen Chun Y, Pai Chi L, Yung Ming J, Hey Chi H, Po Ling K, Meng Lin L, Pei Ming Y and Po Huang L 2002 Elastic modulus measurements of human liver and correlation with pathology *Ultrasound Med. Biol.* **28** 467–74

Wu T, Felmlee J P, Greenleaf J F, Riederer S J and Ehman R L 2001 Assessment of thermal tissue ablation with MR elastography *Magn. Reson. Med.* **45** 80–7